

A Novel Twofold Symmetry Architected Metamaterials with High Compressibility and Negative Poisson's Ratio

Kamran A. Khan,* Mohammad H. Alshaer, and Muhammad Ali Khan

This study presents the compression response of additively manufactured novel soft porous structures with architected microstructure. Six porous additively manufactured architected periodic structures with two-fold and four-fold symmetry were considered. The effect of pore shape and fold symmetry of microstructure on the non-linear response of a square array of architected pores in a soft polymeric matrix is experimentally investigated. The digital image correlation (DIC) is used for investigating the evolution of strains and deformation during uniaxial tensile tests and compression tests of porous structures. Compression induced instability lead to negative Poisson's ratio, and compaction of porous structures, which is found to depend not only on the shape of the architecture but also the fold symmetry exists in the microstructure's unit cell. Unique architectures with multiple buckling modes and shape transformation are also observed. Two-fold symmetry structures are found to buckle at lower strains compared to the four-fold symmetric structure at the same porosity level and produced high compaction and negative Poisson's ratio. The results showed that in addition to pore shape, the fold symmetry could be used effectively to design a new class of soft, active, and reconfigurable devices over a wide range of length scales with desired characteristics.

1. Introduction

The advancements in additive manufacturing (AM) technology make the fabrication of complex architected materials and structures at multiple length scales possible to explore a new family of metamaterial. A metamaterial is an artificially engineered material to have a property not found in conventional materials.^[1] Historically, the term "metamaterials" were limited to electromagnetism field, but, recently, it has been extended to photonic, phononic, and mechanical systems to design architected engineered materials that exhibit properties not usually found in conventional materials.^[2] Mechanical metamaterials refer to a sort of metamaterials that designed artificial structural materials with counterintuitive mechanical properties derived from their tailored internal microstructure rather than the composition of base material.^[3] The unusual properties include negative Poisson's ratio, negative modulus of elasticity, and negative compressibility.^[4,5]

Examples of mechanical metamaterials include acoustic metamaterials, auxetic materials, pentamode metamaterials, and micropolar metamaterials. The concept of metamaterials combined with AM opens new design avenues for the fabrication of complex microstructures over a wide range of length scales.^[6-8]


Auxetic mechanical metamaterials are recognized by a negative Poisson's ratio; i.e., materials will contract (expand) in the transverse direction when compressed uniaxially (stretched). Auxetic mechanical metamaterials are of interest because of their enhanced mechanical properties, such as increased indentation resistance,^[9] shear modulus,^[10] and fracture toughness.^[11] They have a great potential in engineering applications, such as cellular materials with superior damping and acoustic properties,^[12] piezoelectric metamaterials,^[13] piezocomposites,^[14] auxetic fasteners,^[15] bioprostheses,^[16] tissue engineering,^[17] and mechanically tunable, elastically reversible, and transformable topological mechanical metamaterials.^[18,19]

The negative Poisson's ratio of auxetic material depends on the topology of auxetic building blocks and scale-independent.^[20,21] Several natural materials exhibit negative Poisson's ratio, such as silicates,^[22] cubic elemental metals,^[23] zeolites,^[24] natural layered ceramics,^[25] and monolithic ferroelectric polycrystalline ceramics.^[26] Love^[27] was the first to report the negative Poisson's ratio of naturally occurring cubic crystals of

Dr. K. A. Khan
Advanced Digital & Additive Manufacturing Center
Khalifa University of Science and Technology
PO Box 127788, Abu Dhabi, UAE
E-mail: kamran.khan@ku.ac.ae

Dr. K. A. Khan, M. H. Alshaer
Department of Aerospace Engineering
Khalifa University of Science and Technology
PO Box 127788, Abu Dhabi, UAE

Dr. M. A. Khan
Centre of Life Cycle Engineering and Management (CLEM)
School of Aerospace
Transport and Manufacturing
Cranfield University
Cranfield, Bedfordshire MK43 0AL, UK

 The ORCID identification number(s) for the author(s) of this article can be found under <https://doi.org/10.1002/adem.202001041>.

© 2021 The Authors. Advanced Engineering Materials published by Wiley-VCH GmbH. This is an open access article under the terms of the Creative Commons Attribution License, which permits use, distribution and reproduction in any medium, provided the original work is properly cited.

DOI: 10.1002/adem.202001041

pyrite. In contrast, Lakes^[28] was the first to propose artificially engineered auxetic material with a re-entrant auxetic building block. Since then, several artificially designed 2D and 3D architected cellular materials have been proposed to achieve negative values for Poisson's ratio at the macro-,^[29] micro-,^[30] and nano-scale.^[31]

The topology of a porous microstructure can have a periodic or stochastic arrangement in nature.^[32] Periodic cellular materials can have 2D cell configuration such as honeycomb or 3D configuration (crystal symmetry) such as strut-base lattice structures. Design of 2D auxetic metamaterials has been realized through utilizing the different auxetic building blocks, such as auxetic cellular materials with re-entrant structures,^[33,34] chiral microstructures,^[35,36] rotating rigid units,^[37–39] origami structures,^[40] hierarchical laminates,^[41] polymeric and metallic foams,^[42] microporous polymers,^[43] molecular networks,^[44] triangular lattice with cubic symmetry,^[45] a pattern of elongated cuts into an elastomeric sheet,^[46,47] and hexagonal periodic distribution of the elongated perforation.^[48] Similarly, the design of 3D auxetic metamaterials has also been proposed mainly using re-entrant-type auxetic building blocks.^[49–52] Mechanical properties of these 3D auxetic structures were mainly realized via AM technology for both stiff and soft materials.

Auxetic effects in soft architected porous materials are ubiquitous in both natural and man-made systems. There has been a great interest in investigating the 2D and 3D soft metamaterials^[53] due to their ability to mechanical tunability at a low stress level. Recently, AM advancement has been used to design a new family of architected materials using soft lattice structures^[17,54,55] and closed-cell foams.^[56] Soft porous materials with an artificially designed microstructure can undergo large deformation in response to various stimuli that offer a paradigm shift in the design of reconfigurable and on-demand transformable devices,^[18,57] such as the design of metamaterials with negative Poisson's ratio,^[58,59] photonic filters,^[60] and phononic switches.^[61]

Soft periodic structures subjected to compressive stresses experience pattern transformations triggered due to mechanical instability, i.e., buckling.^[62] Several studies showed that introducing a periodic array of architected pores with some specific symmetry in an elastic matrix, buckling of the microstructure can be triggered and can lead to auxetic effects with a negative Poisson ratio. Such mechanical instabilities in 2D periodic porous solids were analyzed at different length scales with various architected microstructures. At the microscale, Xu et al.^[30] exploited re-entrant structures fabricated by soft lithography. Similarly, Singamaneni et al.^[63] proposed cylindrical pores fabricated by interference lithography. At the macroscale, Bertoldi et al.^[58] used cylindrical pores, and Overvelde et al.^[64] proposed the architected fourfold symmetry microstructure fabricated by solution casting, and Babaee et al.^[56,65] proposed 3D soft metamaterials using AM that showed negative Poisson ratios.

The shape of the pore demonstrates a key role in the design and performance of soft periodic materials, as mentioned earlier. However, their nonlinear compression response with fourfold symmetry has been considerably investigated, but the effect of the twofold symmetry on the compressibility and auxeticity response of porous structure still needs a comprehensive investigation. This study presents the compressive deformation

analysis of additively manufactured soft porous architected metamaterials with twofold and fourfold symmetries. A new family of porous architected periodic structures with twofold and fourfold symmetries are proposed. AM based on the Polyjet 3D printing technology was used to fabricate the porous structures using Tango Black Plus soft polymer. The digital image correlation (DIC) was used for investigating the evolution of strains and deformation during uniaxial tensile tests and compression tests of porous structures. Compressive nonlinear response-based uniaxial testing of Tango Black Plus polymer was performed. A compressive deformation analysis of the porous structure was also performed to explore the effect of pore shape and fold symmetry of microstructure on their nonlinear response. The reversible elastic instability caused the pattern transformation that leads to unidirectional negative Poisson's ratio behavior. Compression-induced deformation behavior of the proposed architected porous structures was performed, and several attractive features of soft porous systems, such as critical buckling strain for pattern transformation, buckling modes, compaction response, and negative Poisson's ratio, were computed and analyzed.

2. Description of Porous Architected Structures

The focus of this study is to investigate the pore shape pattern transformation in porous periodic structures under compression. In this study, we created an architecture that consists of a square array of cylindrical through pores in a 3D elastomeric matrix. The planar outer nonintersecting continuous contour of the pore with twofold and fourfold symmetries can be described through Fourier series expansion using the following parametric relations

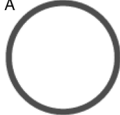
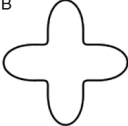
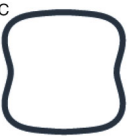
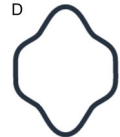
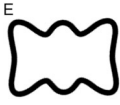

$$x = r(\theta) \cos \theta, y = r(\theta) \sin \theta; \text{ with } 0 \leq \theta \leq 2\pi \quad (1)$$

The contour of the shape and the size of the pore can be controlled using $r(\theta)$, which can be defined by various combinations of Fourier series expansion. We assumed the expression $r(\theta)$ to be a function of $f(r_0, c_1, c_2)$, where r_0 controls the size of the pore to fit within the required dimensions, and c_1 and c_2 control the shape of the pore. In this study, we assumed three different types of expansion to create various families of pores shapes with twofold and fourfold symmetries. **Table 1** shows the Fourier series expansion type, their associated parameters, and the shape of the selected pore. Architectures A and B possess fourfold symmetry; however, architectures C–F have twofold symmetry.

A family of shapes can be obtained using each Fourier series expansion evaluated over a range of c_1 and c_2 and plotted over $0 \leq \theta \leq 2\pi$ to find a nonintersecting closed curve. In this study, we selected two shapes from each expansion to analyze their nonlinear response under compression loading. A 2D design space for each Fourier Series Expansion can also be analyzed by considering different values of c_1 and c_2 within the range shown in Table 1 or beyond, which allows for a systematic study of the effect of shape on the compaction of the porous structures.

As we considered a porous architecture consisting of a square array of cylindrical through pores in a 3D elastomeric matrix, so the size of the pore, r_0 , can be related to the porosity, \emptyset , of the

Table 1. Expression of Fourier series expansions and size of pores, and selected shapes of the pores.

Fourier series expansions	Expression for r_0	Shape of the pores
$r = r_0 \left[\begin{array}{c} 1 \\ +c_1(\cos 2\theta) \\ +c_2(\cos 4\theta) \end{array} \right] \quad \text{(a)}$	$r_0 = \frac{L_0 \sqrt{2\phi}}{P_1}$ $P_1 = \sqrt{\pi(c_1^2 + c_2^2 + 2)}$ <p>Range of $c_1 = c_2 = -0.4, -0.3, \dots 0.4$</p>	<p>A </p> <p>$c_1 = 0,$ $c_2 = 0,$ $P_1 = 1.772$</p> <p>B </p> <p>$c_1 = 0,$ $c_2 = 0.4,$ $P_1 = 1.842$</p>
$r = r_0 \left[\begin{array}{c} 1.5 \\ +c_1(\cos 2\theta) \end{array} \right] c_2 \cos 4\theta \quad \text{(b)}$	$r_0 = \frac{L_0 \sqrt{2\phi}}{P_2}$ <p>Range of $c_1 = c_2 = -0.9, -0.6, \dots 0.9$</p>	<p>C </p> <p>$c_1 = 0.3,$ $c_2 = -0.3,$ $P_2 = 2.530$</p> <p>D </p> <p>$c_1 = 0.6,$ $c_2 = 0.3,$ $P_2 = 2.517$</p>
$r = r_0 \left[\begin{array}{c} 0.4 \\ +c_1(\sin 2\theta) \\ +c_2(\cos 4\theta) \end{array} \right] \sin \theta \cos \theta \quad \text{(c)}$	$r_0 = \frac{L_0 \sqrt{2\phi}}{P_3}$ <p>Range of $c_1 = c_2 = -2.0, -1.0, \dots 2.0$</p>	<p>E </p> <p>$c_1 = 1,$ $c_2 = -2,$ $P_3 = 2.704$</p> <p>F </p> <p>$c_1 = 1,$ $c_2 = 2,$ $P_3 = 2.531$</p>

structure. Considering a cuboid unit cell of edge length of L_0 and depth D enclosing a through pore, then the porosity ϕ of the structure can be obtained using the expression.^[64]

$$\phi = \frac{V_{\text{pore}}}{V_{\text{cell}}} = \frac{A_{\text{pore}} D}{A_{\text{cell}} D} = \frac{\int_0^{2\pi} r(\theta)^2 d\theta}{L_0^2} \quad (2)$$

A general expression of r_0 for expansion (1) is shown in Table 1, whereas the general expression of r_0 cannot be obtained for expansion (b) and (c); therefore, the integrals have to be evaluated numerically by pre-substituting the values of c_1 and c_2 to obtain the relationship of porosity and size of the pore.

In this study, the porous periodic architected elastomeric structures with twofold and fourfold symmetries were considered, consisting of 8×8 unit cells arranged on a square array, and the dimensions of all structures are $80 \text{ mm} \times 80 \text{ mm} \times 15 \text{ mm}$, as shown in **Figure 1a,b**. A representative 2×2 unit cell of a particular pore in a square array is shown in **Figure 1c,d**. The $L_0 = 10 \text{ mm}$ denotes the center-to-center distance between neighboring pores. To preserve the porous structure integrity, the values of c_1 and c_2 have to be chosen, such that $0 \leq x \leq L_0/2$ and $0 \leq y \leq L_0/2$, whereas the constraints of r_{min} , t_{min} , and t_{max} have to be maintained.^[66] However, t_{max} was governed by thickness t_{min} . The shape and size were, therefore,

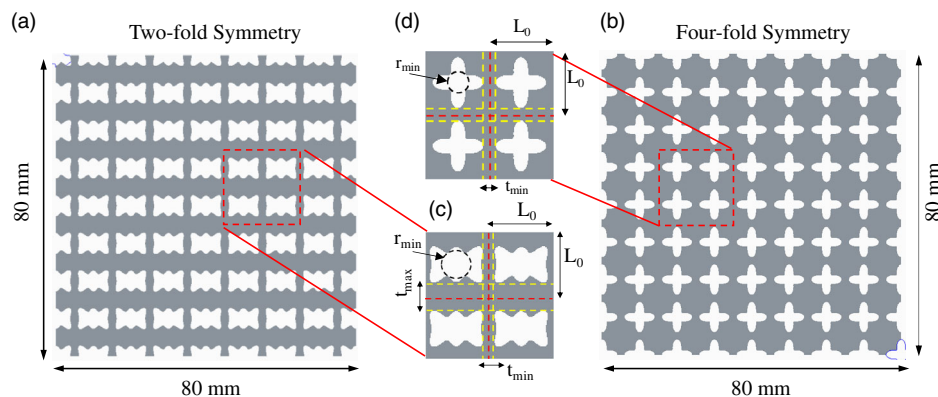


Figure 1. Example of the porous structures with a planar dimension of 80×80 and a depth of $D = 15 \text{ mm}$: a) twofold symmetry and b) fourfold symmetry. A 2×2 unit cell of periodic porous structure with c) twofold symmetry and d) fourfold symmetry, representing the center-to-center distance between the pores L_0 , smallest unit cell dimension L_0 and the constraints variables of a pore (r_{min}), and minimum and maximum distances between the pores (t_{min} and t_{max}).

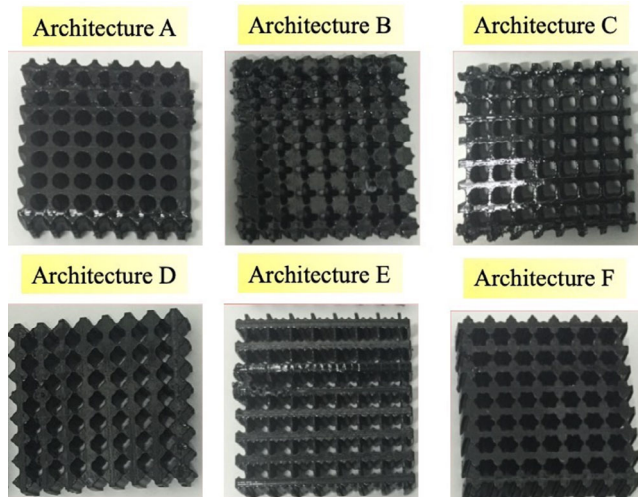


Figure 2. The 3D printed porous periodic architected elastomeric structures with twofold and fourfold symmetries using Tango Black Plus FLX980.

defined using the relation (ϕ_i, c_{1i}, c_{2i}) , where i denotes the architecture name, such as A–F. ϕ represented the porosity and can range from porosity at r_{\min} up to the porosity that yield t_{\min} . In this study, we studied the porous structure with the following specifications. $(\phi_A, c_{1A}, c_{2A}) = (0.46, 0, 0)$, $(\phi_B, c_{1B}, c_{2B}) = (0.36, 0, 40)$, $(\phi_C, c_{1C}, c_{2C}) = (0.46, 0.3, -0.30)$, $(\phi_D, c_{1D}, c_{2D}) = (0.42, 0.6, 0.30)$, $(\phi_E, c_{1E}, c_{2E}) = (0.42, 1.0, -2.0)$, and $(\phi_F, c_{1F}, c_{2F}) = (0.46, 1, 2)$.

3. Fabrication

AM based on the Polyjet 3D printing technology was used to fabricate all test specimens. In Polyjet technology, material or several liquid photopolymers were injected, and 3D physical models were built layer by layer and cured through the exposure of ultraviolet light. In this study, we used the Object260 Connex 3D printer (Stratasys Ltd., USA) and used rubber-like material named Tango Black Plus FLX980, a trademark of Stratasys.^[67] We created 3D computer-aided design (CAD) models for the architected porous structures using a Creo Parametric 3.0

software. The CAD files were exported as a stereolithography (STL) file format, and then transferred to object studio software, which was used as an interface to connect and transfer data to the 3D printer.

The printer had a resolution of 16 μm in the z -direction (depth or printing direction) and 42 μm in the x - and y -directions (planar direction). The 3D printing process-related anisotropy is known to influence the material behavior of printed specimens, although this is not relevant for rubber-like material considered here as a fully cured, fully dense structure with negligible measurable porosity.^[68] All porous structures, including the uniaxial specimens, were manufactured with a layer thickness deposition of 16 μm and an accuracy of 20–85 μm .^[67] **Figure 2** shows all porous architected structures considered in this study. All printed samples were left at room temperature for several days to allow for enough curing. To characterize the mechanical response of the base material, tensile coupons were fabricated according to ASTM D412 type C. Three samples of all tested specimens were printed along the thickness direction (i.e., building direction) of uniaxial and porous structures.

4. Experimental Setup and Strain Analysis

All tests were performed on the Instron 5948 Universal Testing System with a load cell of 100 N.

For uniaxial testing, pneumatic grippers were used to hold the specimen during the testing. Both end tabs of the tensile specimens were bonded with a thin wooden sheet to ensure the proper gripping and preventing the sample from being punctured. The tensile testing of the coupons was performed perpendicular to the printing direction with a crosshead velocity of 20 mm min^{-1} at room temperature until the failure of the sample, as shown in **Figure 3a**. This rate gave a good approximation to the rate-independent response of the material behavior.^[58] A high-resolution digital camera facing the specimen was used to record the video of the testing. The strain analysis was performed using the DIC method. The load associated with the displacement was recorded and used to produce tensile stress–strain curves (Supporting Information).

Compression tests were performed for the porous architected structures in their as-built condition at room temperature. The

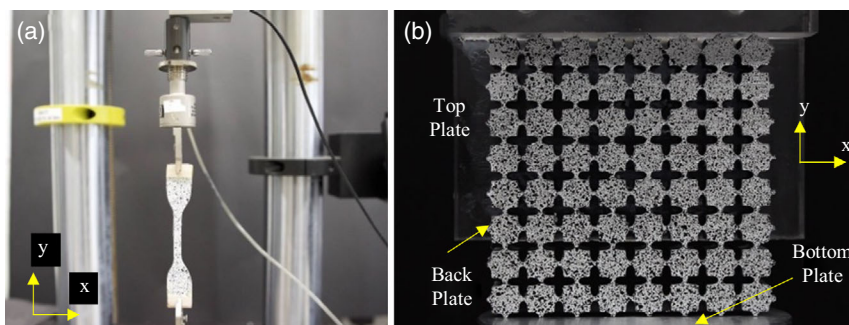


Figure 3. Testing of 3D printed specimens: a) uniaxial testing of coupons and b) compression testing of porous periodic architected elastomeric structures.

porous structures were tested perpendicular to the printing direction, i.e., in the z-direction. According to the coordinates system, as shown in Figure 3b, a particular fixture made of transparent acrylic is designed to perform the compression test, as shown in Figure 3b. The fixture consists of a top flat and a backplate attached to the moving part of the machine. The backplate's purpose was to hold the specimens and prevent out-of-plane buckling during the tests. The bottom plate was attached to the machine on which the specimen of 80 mm width can be easily placed and stand before the test. During the tests, the specimens were not clamped, and the friction between the sample and surface of the fixture was enough to transfer the compressive force and position the specimen. The parallelism of the top and bottom plates was monitored, and grease was used at the mating surfaces of the specimen with the backplate to reduce frictional effects. A Canon EOS 80D camera facing the specimen was used to capture pictures and record videos. All the porous structures were tested at a crosshead velocity of 20 mm min^{-1} and compressed up to 25% engineering strain. A DIC method was used to perform strain analysis. The load associated with the displacement was recorded and used to produce an effective stress–strain diagram for the compression response of porous structures.

4.1. Strain Analysis Procedure

In the test setup, the camera was positioned facing the surface of the specimen. The DIC technique was used for investigating the evolution of strains and deformation during uniaxial tensile tests and compression tests of porous structures.^[69] The specimen's surface was prepared by applying a speckle pattern on the selected region of interests (ROI), produced by applying a thin coating of white matte followed by a random distribution of black dots using spray paint. In this work, the 2D-DIC analysis was performed using the GOM Correlate software. Regarding the size of the ROI, based on the magnification and quality of the average speckle size obtained by spray paint, a facet size of $11 \times 11 \text{ pixels}^2$ was chosen. To avoid statistically correlated

measurements, the facet step was also set to $11 \times 11 \text{ pixels}^2$. For some porous structures where a better acquisition of local effects within the facet was required, a smaller facet size was also adopted. The distance between the individual facets was manipulated from three pixels or less for higher spatial resolution of measurements. The in-plane displacements were then numerically differentiated to determine the strains field. The typical resolution of the measurements was in the range of 10^{-2} mm and 0.01–0.02% for displacement and strain evaluation, respectively.

The ROI for uniaxial testing is shown in **Figure 4a**, and standard procedure is followed to compute the axial and transverse strains. However, to better understand the geometrical changes and transformation of the internal microstructure of porous structures, several parameters were of interest, such as Poisson's ratio, change of the structure planar area, or the changes of porosity under compression. To compute all these parameters, we focused on the behavior of the central region of the specimen, where the boundary condition does not dominate the behavior. We considered the ROI consisting of nine unit cells, as shown in Figure 4b, and the displacement at each vertices shown in Figure 4c of unit cells, and corresponding axial and transverse strains were computed using the DIC. For each unit cell, local values of engineering strain $\varepsilon_{xx}^{[i,j]}$ and $\varepsilon_{yy}^{[i,j]}$ were computed from the DIC analysis. The local Poisson's ratio $\nu^{[i,j]}$ is defined as

$$\nu^{[i,j]} = -\frac{\varepsilon_{xx}^{[i,j]}}{\varepsilon_{yy}^{[i,j]}} \quad (3)$$

and compaction $\psi^{[i,j]}$ may be expressed as

$$\psi^{[i,j]} = \frac{A_0^{[i,j]} - A^{[i,j]}}{A_0^{[i,j]}} = 1 + \left(1 + \varepsilon_{xx}^{[i,j]}\right)\left(1 + \varepsilon_{yy}^{[i,j]}\right) \quad (4)$$

where $A_0^{[i,j]}$ and $A^{[i,j]}$ denote the area of unit cell in initial and current configuration. The ensemble averages for all nine unit cells under consideration can be expressed as $\bar{\varepsilon}_{xx} = \langle \varepsilon_{xx}^{[i,j]} \rangle$, $\bar{\varepsilon}_{yy} = \langle \varepsilon_{yy}^{[i,j]} \rangle$, $\bar{\nu} = \langle \nu^{[i,j]} \rangle$, and $\bar{\psi} = \langle \psi^{[i,j]} \rangle$.

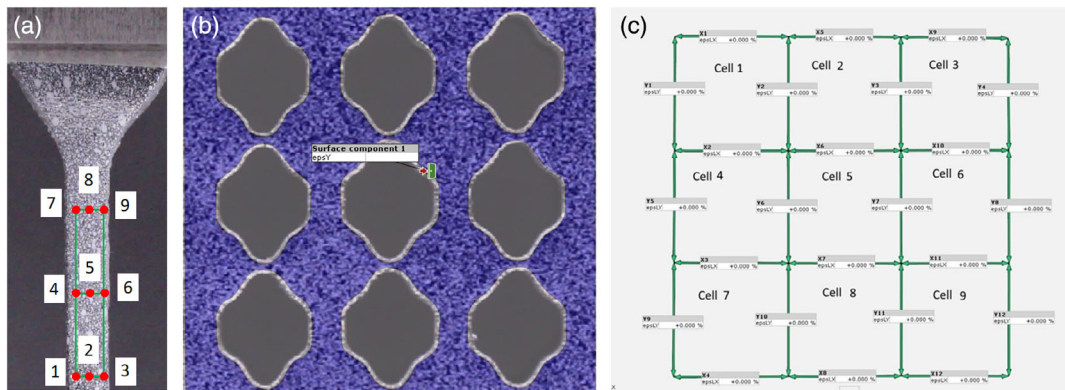


Figure 4. DIC of specimens: a) ROI during uniaxial testing of coupons, b) ROI consisting of nine unit cells during compression testing of porous structures, and c) labeling of nine unit cells showing the locations of 16 vertices and wall of each unit cell for measuring local axial and transverse engineering strain in the x- and y-directions for each unit cell.

5. Experiment Results

5.1. Architected Metamaterials

In this section, we experimentally analyzed the porous microstructure's evolution during the uniaxial compression tests at different levels of applied engineering strains (ϵ). **Figure 5** shows the microstructures of all six porous structures at different levels of applied engineering strain ϵ . All structures were uniaxially compressed up to an engineering strain of 25%. We opted three levels of strains, i.e., $\epsilon = 0.00$, 12.5%, and 25%, to see the evolution of microstructures. For both types of structures, i.e., twofold and fourfold symmetries, we observed buckling-induced changes in the microstructures that take place suddenly after a critical value of the compressive strain. However, the mode of buckling in all microstructures depends on the shape of the pores and fold symmetries.

Figure 5b shows that all porous structures buckled before 12.5% strain until except architectures A and D. To better compare the types of fold symmetry, consider an architecture with a similar porosity of $\phi = 46\%$, i.e., A, C, and F. It is clearly shown in Figure 5b that both architectures C and F that possess twofold symmetries buckled before 12.5% strain despite the same level of porosity as compared with architecture A. However, the mode of buckling did depend on the shape of the pore. In architectures A, B, D, and F, the buckling mode was characterized by a wavelength equal to twice the unit cell ($2L_0$) in both horizontal and vertical directions and always leads to the formation of a checkerboard pattern. In architectures C and E, the structural instability was characterized by a wavelength equal to the height of the sample and showed twinning-like phase transformation behavior as observed in shape memory alloys.^[70]

Figure 5c shows the microstructure state at 25% strain and can be seen that the further compression leads to further compaction of the microstructures. However, microstructure shape was fully recovered upon unloading, as the strain at each material point in the porous structure was in elastic range (see Figure S1, Supporting Information). It was observed that when the buckling

mode was of unit cell scale, some interesting effects such as lateral contraction and localized compaction were observed, resulting in the complete closure of the central portion of the microstructure. By contrast, when the buckling mode was of porous structure height, very low levels of compactions were observed. At a strain level of 25%, architectures A and F lead to a similarly high compaction level, but the complete closure of the pores was not observed. However, architecture D shows more closure of pores with the highest compaction level and demonstrates the importance of pore shape and symmetry in designing soft porous architected structures.

To better understand the evolution of the microstructure, their different stages observed during compression can be analyzed using a close examination of the effective stress–strain behavior shown in **Figure 6**. Architectures A and E buckled at very high- and low-stress values, respectively. At the same level of porosity, all twofold structures showed instability at lower critical strain values. In typical cellular solids, three distinct regimes during compression tests were observed,^[71] i.e., linear elastic regime, stress plateau, and densification. By contrast, we observed three

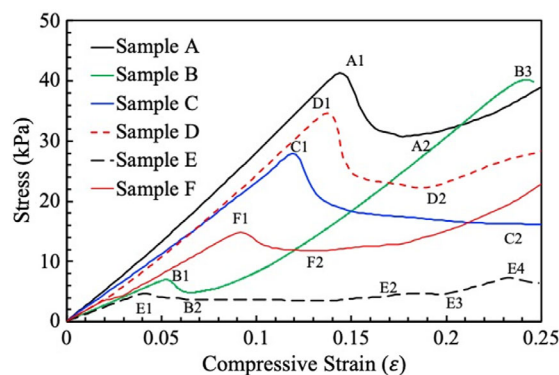


Figure 6. Effective stress–strain behavior of architected porous microstructures as a function of applied engineering strains highlighting different states of microstructure during the compression tests.

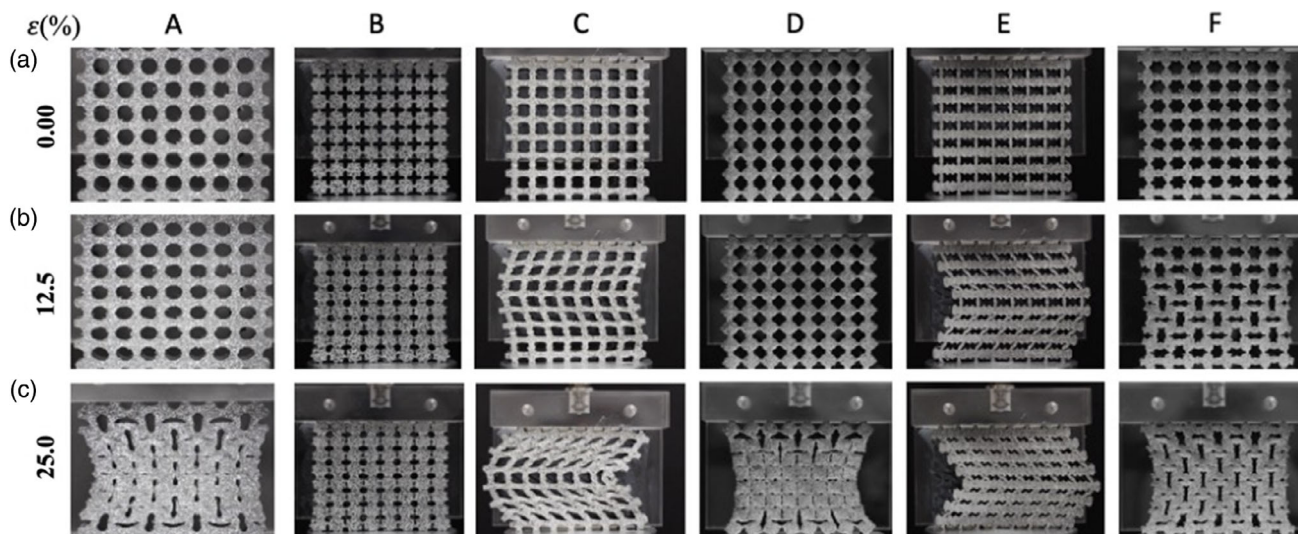


Figure 5. Deformation pattern and evolution of microstructure of architected porous microstructures at different levels of applied engineering strains.

categories of compression stress–strain responses for all porous structures. In the first category (similar to typical cellular solids), the stress–strain behavior showed that there were mainly three stages during the compression of porous structures; i.e., during the first stage, the porous structure compresses, and after reaching a critical strain, instability occurs.

Figure 6 shows labels A_1 , B_1 , C_1 , D_1 , E_1 , and F_1 that denote the state at which instability starts. In the second stage, the microstructure continued to deform at a lower level of stress and after reaching a certain compaction level where few of the surfaces came into contact with each other. A_2 , B_2 , C_2 , D_2 , E_2 , and F_2 denote the contact state. In the third stage, more stress was required to compress the porous structures further. The three-stage behavior was observed in architectures A, D, and F. In the second category, in addition to three stages, there is a fourth stage in which the structure buckled again at the second level of critical strain. This type of structure possessed multiple buckling patterns and was observed in architectures B and E. B_3 and E_4 denote the state at which another instability occurs. It should be noted that architecture B possesses fourfold symmetry, whereas architecture E has twofold symmetry. So, it is possible to design soft porous architected structures that show buckling behavior at two different compaction stages. In the third category, there were only two stages observed during compression, and once the critical strain reaches, the stress level continuously decreases while the structure compresses with transverse displacement. However, at very high compressive strain, it was expected that either the third stage might be activated or an out-of-plane deformation-induced buckling occurred. Only, architecture C showed two-stage compression behavior.

As clearly shown in Figure 5, the nature of buckling was different from one structure to another. Next, we analyzed the load at which instability occurs. Consider all architectures with a similar porosity of $\varnothing = 46\%$, i.e., A, C, and F, but possesses different fold symmetries. In the literature, it was shown that the hole has a strong effect on mechanical instability. When the structure was characterized by microscopic instabilities, more stress was required to buckle the porous structure compared with the case when the structure showed macroscopic instability (i.e., a buckling mode characterized by a wavelength larger than the size of microstructure).^[53] However, in this study, when comparing the porous structure with twofold symmetry, we observed that the structure characterized by microscopic instability (i.e., architecture F) required less stress to buckle the porous structure as compared with a structure that shows macroscopic instability (i.e., architecture C), as shown in Figure 6.

Next, we analyzed the microstructural features in different architectures at critical strain state and lowest stress state during compression testing, i.e., the state at which the internal surfaces of the microstructure touch each other and after which the stresses tend to increase. Figure 7a shows the overlap pictures at $\varepsilon = 0.00\%$ and strain state at A_1 (i.e., overlap picture in light green color). It can be seen by a red arrow that when buckling starts, the circles started to become an ellipse. At strain state A_2 , some of the transformed ellipse internal surfaces started to come into contact, as shown in Figure 7b, and further compression after A_2 led to a rise in stress. Figure 7c,d shows the deformation state of architecture B. It can be seen that the transformation of the shapes started at state B_1 (overlap picture in light yellow color), whereas at strain state B_2 , the surfaces came into contact,

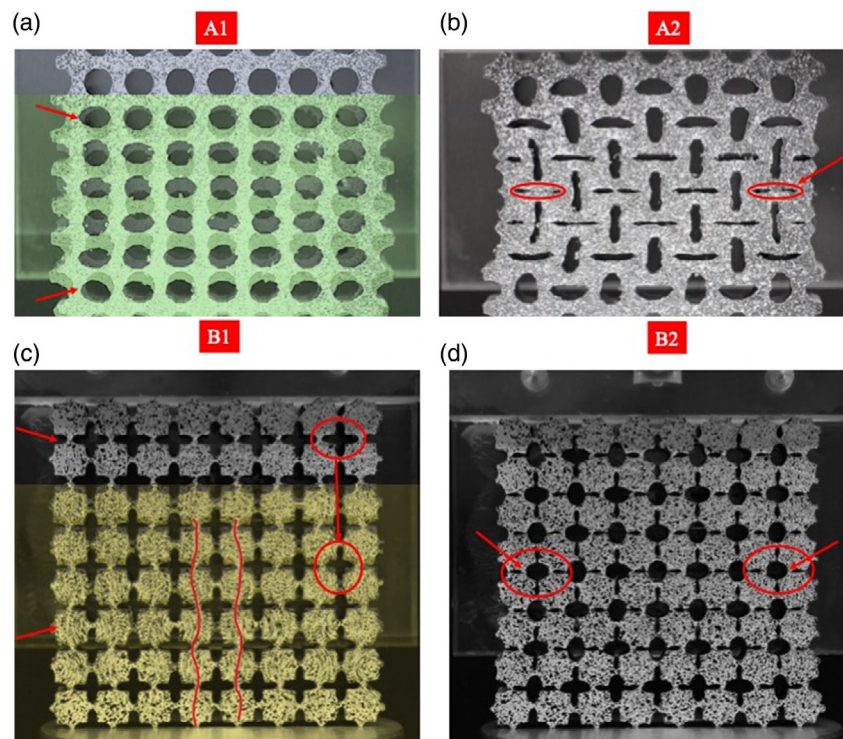


Figure 7. Buckling and stiffening mechanism of architected porous microstructures A and B at different states of microstructure during the compression tests.

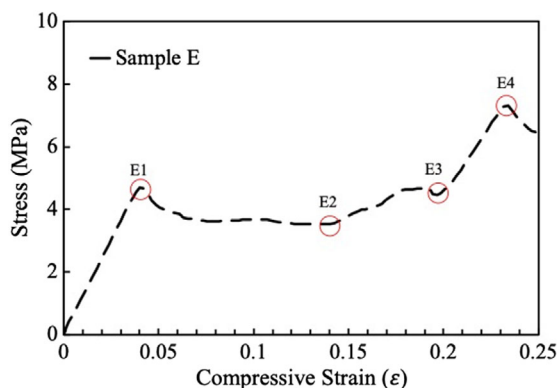


Figure 8. Stress-strain plots of architected porous microstructure E during the compression tests.

and further compression may lead to an increase in stress as shown with red color lines. Figure 7a,c clearly shows that for both architectures, the buckling mode can be characterized by a wavelength equal to twice the length of the unit cell ($2L_0$) in both horizontal and vertical directions (**Figure 8**).

Next, we analyzed the microstructure's evolution of architecture E at different compressive strain levels, as shown in **Figure 9**. The stress-strain diagram was marked with four different states of strain that showed different stages during the compression of porous structures. Figure 9a shows the microstructure when the critical strain is reached, E_1 . The yellow line shows that the structure experienced macroscopic instability, and its buckling mode was characterized by a wavelength equal to the size of the microstructure. At the lowest stress level referred as state E_2 , as shown in Figure 9b, it can be seen that the strut at

the center did not start to buckle, whereas all the microstructures above and below showed the twinning-like transformation behavior. Figure 9c shows the architecture at strain state E_3 , which shows the sudden drop in the stress due to the buckling of strut as shown with a red arrow in top-right and bottom-right locations of the porous structure. There was a load increase observed between states E_3 and E_4 due to the stress required to close the pores. Figure 9d shows the architecture strain state at E_4 where it can be seen that instability of the central strut took place that caused a further drop in the stress level, as shown in Figure 9.

Next, we present the DIC results to investigate the evolution of strains and deformation during uniaxial compression tests of all porous structures. Based on the ensemble engineering strain calculations within nine unit cells at the center of the microstructure, a more quantitative comparison between the responses of all porous structures was made by inspecting negative Poisson's ratio and compaction behavior. **Figure 10a** presents the microstructure's evolution as a function of the applied engineering strain ϵ . The microstructure results are shown at three different strain states, i.e., at the start of test, at instability, and at the strain state that yields the lowest stress. At a higher compaction level, the localized engineering strain reached a higher value, closer to 30%, which was more than the applied global engineering strain. The regions usually where the highest bending occurred show such strain behavior and can be seen in red color at different locations in all porous structures.

Figure 10b shows the evolution of Poisson's ratio $\bar{\nu}$ as a function of the local engineering strain $\bar{\epsilon}_{yy}$. The lateral contraction was strongly dependent on the buckling mode, and the difference between different structures was remarkable. When the

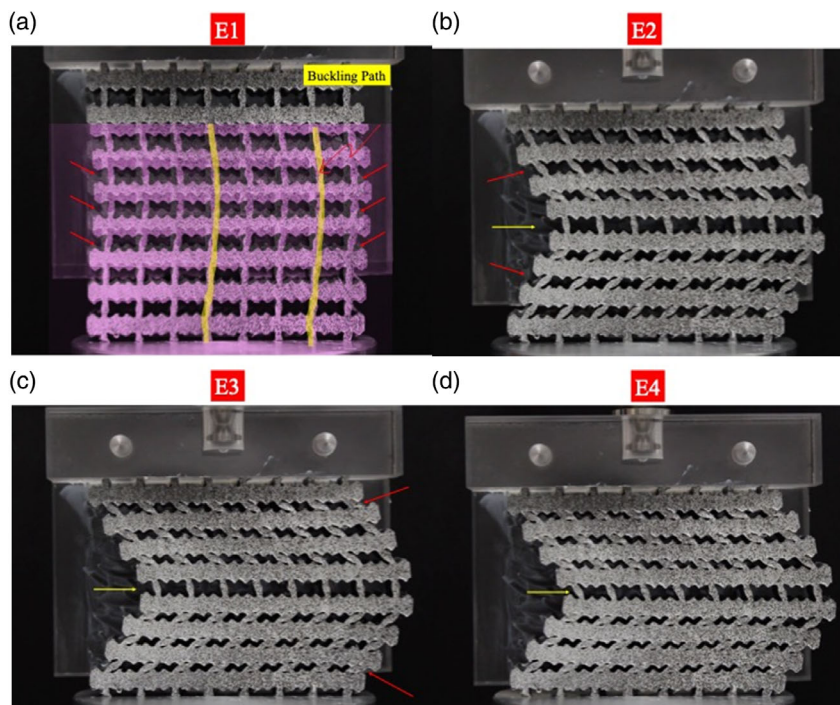


Figure 9. Buckling and stiffening mechanism of architected porous microstructure E during the compression tests.

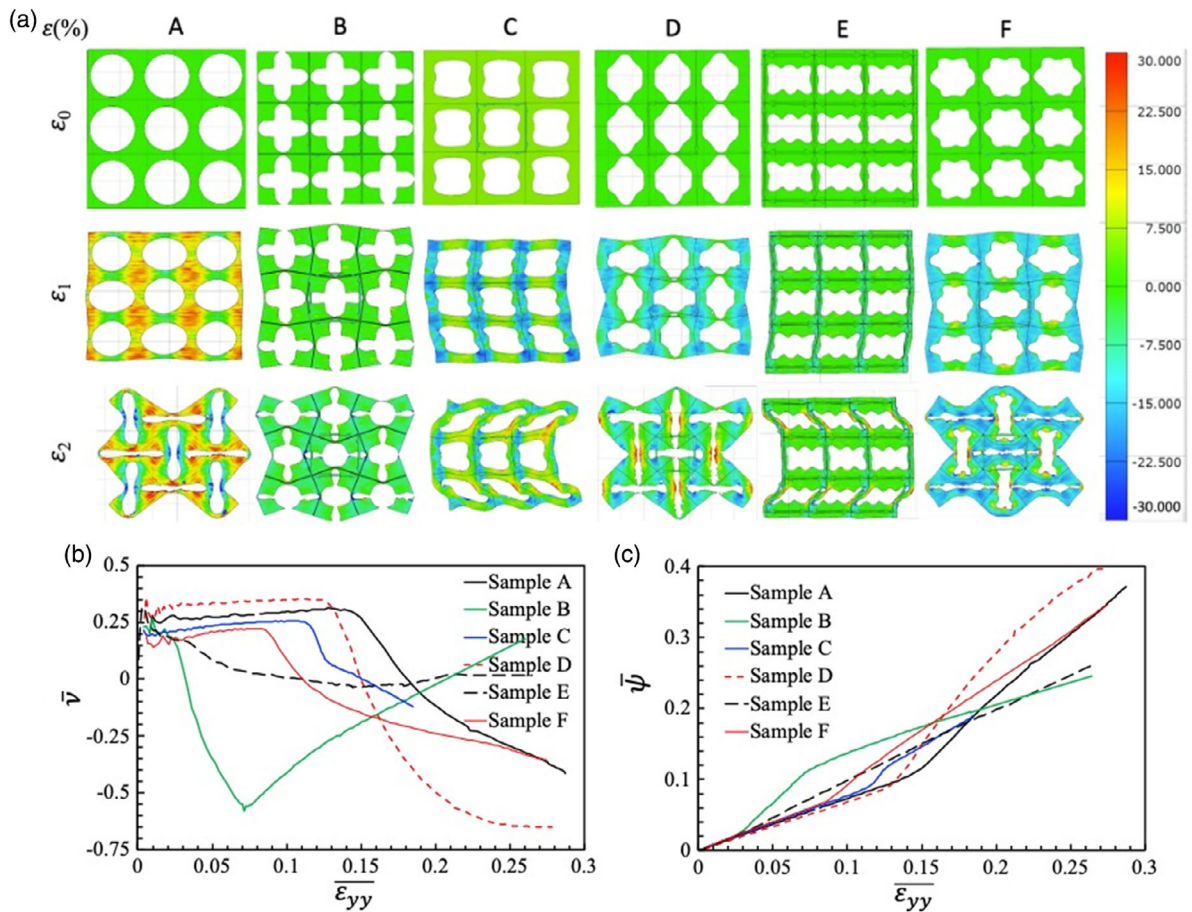


Figure 10. a) DIC results of engineering strain within nine unit cells at the center of the microstructure showing the deformation pattern and evolution of microstructure of architected porous structures at different levels of applied engineering strains. b) Poisson's ratio and c) compressibility response, as a function of ensemble engineering strain nine unit cells at the center of the porous microstructure.

structures were characterized by microscopic instability (architectures A, B, D, and F), significant lateral contraction induced by buckling was observed, leading to high negative values of Poisson's ratio. On the other hand, when the structure showed macroscopic instability (architectures C and E), Poisson's ratio of the structures was marginally affected by deformation and buckling. Moreover, it is interesting to observe that the lateral contraction in architecture D was remarkably larger than in all other architectures, leading to the largest negative values of Poisson's ratio. Among the twofold and fourfold symmetric structures at the same porosity level (A, C, and F), architectures A and F showed similar values of the largest negative Poisson's ratio. For architectures B and E, initially sharp lateral contraction led to negative Poisson's ratio, but further compression led it to positive Poisson's ratio for both architectures. Architecture B showed a very high negative Poisson's ratio, whereas architecture E showed Poisson's ratio close to zero.

The evolution of the compaction $\bar{\nu}$ for all porous structure is shown in Figure 10c as a function of local average engineering strains. All structures followed a similar rate of compaction until the instability occurs in a microstructure. Architectures A and C showed two transitions of compaction rate, whereas all other architectures showed just one transition. As architecture A shows

instability at very low strain, it was the first to show the transition in compaction, whereas architecture A was the last one to show a transition in compaction rate. The architecture with microscopic instability showed more compressibility as compared with porous structures that showed macroscopic instability. However, the twofold symmetry architecture (D) showed the highest compaction, followed by the fourfold symmetry architecture (A). We observed experimental results for one porosity; however, at lower porosity, limited compressibility with macroscopic instability was observed, and a very high porous structure led to fragile specimens with very thin ligaments. These results showed that instabilities could be used to design soft novel architected porous metamaterials, whereas pore shapes and fold symmetries can also be utilized to design tunable metamaterials with controllable Poisson's ratio and compressibility response.

6. Conclusion

We presented the compression response of soft architected porous metamaterials in this article. A new class of novel 2D architectures with the twofold and fourfold symmetry microstructures were proposed. Unlike rigid ligaments-based cellular

solids, the porous structures consist of a periodic square array of 2D soft continuous architected pores in the elastomeric matrix. Under mechanical compression, all porous structures showed elastic instability that led to negative Poisson's ratio and controllable porosity. As compared with circular porosity, architecture D showed larger negative Poisson's ratio and higher compressibility behavior. At the same porosity level, a twofold symmetry structure showed instability at lower loads. In both the twofold and fourfold symmetric microstructures, we observed two buckling modes spanning over multiple unit cells or the size of the porous microstructures. The porous structures whose buckling mode wavelength was characterized by the length of unit cells showed a higher negative Poisson's ratio than the others. It was shown that the architected pore shape and the fold symmetry could be used to design a new class of soft, fast reversible porous actuators, and reconfigurable devices over a wide range of length scales. Soft porous systems can be designed with desired properties and controllable features, such as their stiffness, critical buckling strain, multiple buckling modes, compaction level, and negative Poisson's ratio.

Supporting Information

Supporting Information is available from the Wiley Online Library or from the author.

Acknowledgements

This publication was based on work supported by the Khalifa University of Science and Technology under Award No. CIRA-2018-15 and Abu Dhabi Award for Research Excellence (AARE-2019) under project number 8434000349.

Conflict of Interest

The authors declare no conflict of interest.

Data Availability Statement

Research data are not shared.

Keywords

auxetic smart structures, cellular materials, instabilities, metamaterials, porous structures

Received: September 3, 2020

Revised: February 8, 2021

Published online:

- [1] Z. G. Nicolaou, A. E. Motter, *Nat. Mater.* **2012**, *11*, 608.
 [2] A. A. Zadpoor, *Mater. Horiz.* **2016**, *3*, 371.
 [3] T. J. Cui, R. Liu, D. R. Smith, *Metamaterials - Theory, Design, and Applications*, 1st ed., (Eds: T. J. Cui, D. Smith, R. Liu), Springer, Boston, MA **2010**.
 [4] J. N. Grima, R. Caruana-Gauci, *Nat. Mater.* **2012**, *11*, 565.

- [5] J. U. Surjadi, L. Gao, H. Du, X. Li, X. Xiong, N. X. Fang, Y. Lu, *Adv. Eng. Mater.* **2019**, *21*, 1800864.
 [6] J. Chen, K. Wang, C. Zhang, B. Wang, *Addit. Manuf.* **2018**, *24*, 341.
 [7] J.-H. Lee, J. P. Singer, E. L. Thomas, *Adv. Mater.* **2012**, *24*, 4782.
 [8] K. Wang, C. Wu, Z. Qian, C. Zhang, B. Wang, M. A. Vannan, *Addit. Manuf.* **2016**, *12*, 31.
 [9] R. S. Lakes, K. Elms, *J. Compos. Mater.* **1993**, *27*, 1193.
 [10] X. Huang, S. Blackburn, *Key Eng. Mater.* **2002**, 206–213, 201.
 [11] J. B. Choi, R. S. Lakes, *Int. J. Fract.* **1996**, *80*, 73.
 [12] F. Scarpa, L. G. Ciffo, J. R. Yates, *Smart Mater. Struct.* **2003**, *13*, 49.
 [13] K. A. Khan, S. Al-Mansoor, S. Z. Khan, M. A. Khan, *J. Eng. Mech.* **2019**, *145*, 04019101.
 [14] O. Sigmund, S. Torquato, I. A. Aksay, *J. Mater. Res.* **1998**, *13*, 1038.
 [15] J. B. Choi, R. S. Lakes, *Des. Fasten. Based Negat. Poissons Ratio Foam* **1991**, *10*, 205.
 [16] F. Scarpa, *IEEE Signal Process. Mag.* **2008**, *25*, 128.
 [17] P. Mardling, A. Alderson, N. Jordan-Mahy, C. L. L. Maitre, *Biomater. Sci.* **2020**, *8*, 2074.
 [18] J.-H. Jang, C. K. Ullal, T. Gorishnyy, V. V. Tsukruk, E. L. Thomas, *Nano Lett.* **2006**, *6*, 740.
 [19] D. Z. Rocklin, S. Zhou, K. Sun, X. Mao, *Nat. Commun.* **2017**, *8*, 14201.
 [20] H. M. A. Kolken, A. A. Zadpoor, *RSC Adv.* **2017**, *7*, 5111.
 [21] K. E. Evans, *Endeavour* **1991**, *15*, 170.
 [22] A. Yeganeh-Haeri, D. J. Weidner, J. B. Parise, *Science* **1992**, *257*, 650.
 [23] R. H. Baughman, J. M. Shacklette, A. A. Zakhidov, S. Stafström, *Nature* **1998**, *392*, 362.
 [24] J. N. Grima, R. Gatt, V. Zammit, J. J. Williams, K. E. Evans, A. Alderson, R. I. Walton, *Natrolite: A Zeolite with Negative Poisson's Ratios*, American Institute Of Physics, College Park, MD **2007**.
 [25] F. Song, J. Zhou, X. Xu, Y. Xu, Y. Bai, *Phys. Rev. Lett.* **2008**, *100*, 245502.
 [26] X. Tan, W. Jo, T. Granzow, J. Frederick, E. Aulbach, J. Rödel, *Appl. Phys. Lett.* **2009**, *94*, 042909.
 [27] A. E. H. Love, *A Treatise on the Mathematical Theory of Elasticity*, Courier Corporation, North Chelmsford, MA **1944**.
 [28] R. Lakes, *Science* **1987**, *235*, 1038.
 [29] C. Li, H. Lei, Z. Zhang, X. Zhang, H. Zhou, P. Wang, D. Fang, *Addit. Manuf.* **2020**, *34*, 101172.
 [30] B. Xu, F. Arias, S. T. Brittain, X.-M. Zhao, B. Grzybowski, S. Torquato, G. M. Whitesides, *Adv. Mater.* **1999**, *11*, 1186.
 [31] L. J. Hall, V. R. Coluci, D. S. Galvão, M. E. Kozlov, M. Zhang, S. O. Dantas, R. H. Baughman, *Science* **2008**, *320*, 504.
 [32] K. A. Khan, R. K. Abu Al-Rub, *Int. J. Mech. Sci.* **2017**, *126*, 106.
 [33] J. B. Choi, R. S. Lakes, *J. Mater. Sci.* **1992**, *27*, 4678.
 [34] J. Schwerdtfeger, F. Schury, M. Stingl, F. Wein, R. F. Singer, C. Körner, *Phys. Status Solidi B* **2012**, *249*, 1347.
 [35] D. M. Prall, R. S. Lakes, *J. Mech. Sci.* **1997**, *39*, 305.
 [36] F. Scarpa, S. Blain, T. Lew, D. Perrott, M. Ruzzene, J. R. Yates, *Compos. Part Appl. Sci. Manuf.* **2007**, *38*, 280.
 [37] E. Chetcuti, B. Ellul, E. Manicaro, J.-P. Brincat, D. Attard, R. Gatt, J. N. Grima, *Phys. Status Solidi B* **2014**, *251*, 297.
 [38] R. Gatt, L. Mizzi, J. I. Azzopardi, K. M. Azzopardi, D. Attard, A. Casha, J. Briffa, J. N. Grima, *Sci. Rep.* **2015**, *5*, 8395.
 [39] J. N. Grima, A. Alderson, K. E. Evans, *Phys. Status Solidi B* **2005**, *242*, 561.
 [40] M. Schenk, S. D. Guest, *Proc. Natl. Acad. Sci.* **2013**, *110*, 3276.
 [41] G. W. Milton, *J. Mech. Phys. Solids* **1992**, *40*, 1105.
 [42] E. A. Friis, R. S. Lakes, J. B. Park, *J. Mater. Sci.* **1988**, *23*, 4406.
 [43] B. D. Caddock, K. E. Evans, *J. Phys. Appl. Phys.* **1989**, *22*, 1877.
 [44] K. E. Evans, M. A. Nkansah, I. J. Hutchinson, S. C. Rogers, *Nature* **1991**, *353*, 124.
 [45] M. C. Rechtsman, F. H. Stillinger, S. Torquato, *Phys. Rev. Lett.* **2008**, *101*, 085501.

- [46] S. Shan, S. H. Kang, Z. Zhao, L. Fang, K. Bertoldi, *Extreme Mech. Lett.* **2015**, 4, 96.
- [47] M. Taylor, L. Francesconi, M. Gerendás, A. Shanian, C. Carson, K. Bertoldi, *Adv. Mater.* **2014**, 26, 2365.
- [48] G. Carta, M. Brun, A. Baldi, *Mech. Mater.* **2016**, 97, 67.
- [49] K. A. Khan, M. A. Khan, *Mater. Res. Bull.* **2019**, 112, 194.
- [50] X. Ren, J. Shen, P. Tran, T. D. Ngo, Y. M. Xie, *Mater. Des.* **2018**, 139, 336.
- [51] K. Wang, Y.-H. Chang, Y. Chen, C. Zhang, B. Wang, *Mater. Des.* **2015**, 67, 159.
- [52] L. Yang, O. Harrysson, H. West, D. Cormier, *Int. J. Solids Struct.* **2015**, 69–70, 475.
- [53] K. Bertoldi, V. Vitelli, J. Christensen, M. van Hecke, *Nat. Rev. Mater.* **2017**, 2, 1.
- [54] J.-H. Park, K. Park, *Addit. Manuf.* **2020**, 33, 101148.
- [55] M. H. Yousuf, W. Abuzaid, M. Alkhader, *Addit. Manuf.* **2020**, 35, 101364.
- [56] S. Babaee, J. Shim, J. C. Weaver, E. R. Chen, N. Patel, K. Bertoldi, *Adv. Mater.* **2013**, 25, 5044.
- [57] S. Singamaneni, V. V. Tsukruk, *Soft Matter* **2010**, 6, 5681.
- [58] K. Bertoldi, P. M. Reis, S. Willshaw, T. Mullin, *Adv. Mater.* **2010**, 22, 361.
- [59] L. Francesconi, A. Baldi, X. Liang, F. Aymerich, M. Taylor, *Extreme Mech. Lett.* **2019**, 26, 1.
- [60] D. Krishnan, H. T. Johnson, *J. Mech. Phys. Solids* **2009**, 57, 1500.
- [61] J.-H. Jang, C. Y. Koh, K. Bertoldi, M. C. Boyce, E. L. Thomas, *Nano Lett.* **2009**, 9, 2113.
- [62] T. Mullin, S. Deschanel, K. Bertoldi, M. C. Boyce, *Phys. Rev. Lett.* **2007**, 99, 084301.
- [63] S. Singamaneni, K. Bertoldi, S. Chang, J.-H. Jang, S. L. Young, E. L. Thomas, M. C. Boyce, V. V. Tsukruk, *Adv. Funct. Mater.* **2009**, 19, 1426.
- [64] J. T. B. Overvelde, S. Shan, K. Bertoldi, *Adv. Mater.* **2012**, 24, 2337.
- [65] T. Bückmann, N. Stenger, M. Kadic, J. Kaschke, A. Frölich, T. Kennerknecht, C. Eberl, M. Thiel, M. Wegener, *Adv. Mater.* **2012**, 24, 2710.
- [66] J. T. B. Overvelde, K. Bertoldi, *J. Mech. Phys. Solids* **2014**, 64, 351.
- [67] Stratasys, <http://www.stratasys.com/>, Stratasys, USA (accessed: 2015).
- [68] A. S. Dalaq, D. W. Abueidda, R. K. Abu Al-Rub, *Compos. Part Appl. Sci. Manuf.* **2016**, 84, 266.
- [69] L. Francesconi, A. Baldi, G. Dominguez, M. Taylor, *Exp. Mech.* **2020**, 60, 93.
- [70] P. K. Kumar, D. C. Lagoudas, *Introduction to Shape Memory Alloys*, Springer, Boston, MA **2008**, pp. 1–51.
- [71] L. J. Gibson, M. F. Ashby, *Cellular Solids: Structure and Properties*, Cambridge University Press, Cambridge **1997**.

A novel twofold symmetry architected metamaterials with high compressibility and negative Poisson's ratio

Khan, Kamran Ahmed

2021-02-28

Attribution 4.0 International

Khan KA, Alshaer MH, Khan MA. (2021) A novel twofold symmetry architected metamaterials with high compressibility and negative Poisson's ratio. *Advanced Engineering Materials*, Volume 23, Issue 5, May 2021, Article number 2001041

<https://doi.org/10.1002/adem.202001041>

Downloaded from CERES Research Repository, Cranfield University